Terr. Atmos. Ocean. Sci., Vol. 30, No. 3, 367-376, June 2019 doi: 10.3319/TAO.2018.11.15.01

Multiple-event analysis of the 2018 M_L 6.2 Hualien earthquake using source time functions

Ruey-Der Hwang[1,*], Chiung-Yao Lin[1], Cai-Yi Lin[1], Wen-Yen Chang[2], Tzu-Wei Lin[3], Yi-Ling Huang[4], and Jo-Pan Chang[5]

[1] *Department of Geology, Chinese Culture University, Taipei City, Taiwan*
[2] *Department of Natural Resources and Environmental Studies, National Dong Hwa University, Hualien County, Taiwan*
[3] *Seismological Center, Central Weather Bureau, Taipei City, Taiwan*
[4] *Institute of Applied Geosciences, National Taiwan Ocean University, Keelung, Taiwan*
[5] *Center for General Education, National University of Tainan City, Tainan City, Taiwan*

Article history:
Received 31 July 2018
Revised 22 October 2018
Accepted 15 November 2018

Keywords:
2018 Hualien earthquake, Multiple-event analysis, Source time function, Rupture velocity, Static stress drop

Citation:
Hwang, R.-D., C.-Y. Lin, C.-Y. Lin, W.-Y. Chang, T.-W. Lin, Y.-L. Huang, and J.-P. Chang, 2019: Multiple-event analysis of the 2018 M_L 6.2 Hualien earthquake using source time functions. Terr. Atmos. Ocean. Sci., 30, 367-376, doi: 10.3319/TAO.2018.11.15.01

ABSTRACT

Through forward multiple-event analysis of teleseismic P-waves using source time functions (STFs), derived by non-negative time-domain deconvolution, we inferred the rupture features of the 2018 Hualien earthquake. At least six sub-events composed the Hualien earthquake, with the largest one (corresponding to M_w = 6.3) occurring 4.8 s later than the initiation of rupture. The total seismic moment (M_0) of 6.48×10^{18} Nm (M_w = 6.5) and radiated seismic energy (E_S) of 1.76×10^{14} Nm led to the E_S/M_0 ratio ~2.72×10^{-5}. A static stress drop ($\Delta\sigma_S$) of 5.03 MPa was also derived for the earthquake. On average, the rupture parameters of the 2018 Hualien earthquake from this study were similar to globally average values. From M_0 and source duration (10.9 s), this implied an average rupture velocity (Vr) less than 2.0 km s^{-1}. The forward multiple-event modeling showed that $\Delta\sigma_S$ varied with the sub-events and increased with E_S/M_0 to imply the frictional strength being heterogeneous along the fault. From the highest STF peak (6.9 s after the initiation) near the land-sea interface, we suggested that the Hualien earthquake be divided into two rupture processes. One with low $\Delta\sigma_S$, low E_S/M_0, and high Vr occurred at sea; the other with high $\Delta\sigma_S$, high E_S/M_0, and low Vr occurred on land. Both seawater and local velocity structures probably played crucial factors behind these rupture discrepancies during the 2018 Hualien earthquake.

1. INTRODUCTION

On 6 February 2018, a moderate-sized earthquake occurred offshore Hualien in eastern Taiwan (Fig. 1). It caused the destruction of several buildings along the Milun fault and loss of life. Initially, the Central Weather Bureau (CWB) reported that the earthquake had M_L = 6.0, a focal depth of 10 km, and an epicenter at 24.14°N and 121.69°E, which is relatively close to that of the M_L 7.3 Hualien earthquake that occurred on 22 October 1951, at 03:29 (UTC) (Cheng et al. 1997). The location of the 2018 Hualien earthquake appeared to be the forefront of the subduction zone, in which the Philippine Sea plate is subducting beneath the Eurasian plate in a northward direction. The aftershock distribution indicated that the earthquake ruptured southwestward from its epicenter and had almost terminated by the southernmost portion of the Milun fault, as shown in Fig. 1. The focal mechanisms proposed by several organizations demonstrated that a westward-dipping plane with strikes of 208 - 220°, which was consistent with the aftershock distribution, might have been the fault plane on which the 2018 Hualien earthquake occurred (Fig. 1). Through geological survey, however, the Milun fault was interpreted to be a left-lateral strike-slip fault dipping eastward at a high angle (Cheng et al. 1997; Shyu et al. 2016). This resulted in a remarkable controversy regarding whether the 2018 Hualien earthquake occurred on the Milun fault. A field survey revealed that the largest deformation on land was in the northernmost section of the Milun fault; however, the surface vertical offset was absent in the middle portion of this fault; the surface

* *Corresponding author*
E-mail: hrd@faculty.pccu.edu.tw

vertical offset was observed again in the southernmost section (Yen 2018). Historical records indicated that the 1951 M_L 7.3 Hualien earthquake ever ruptured the Milun fault to cause a rupture length of approximately 21 km (cf. Shyu et al. 2016). Probably, the occurrence of the 2018 Hualien earthquake was related to the Milun fault. However, here we concentrated on investigating the rupture features of the Hualien earthquake rather than probing into whether it occurred on the Milun fault.

Imaging the source rupture process provides not only information about the physics of an earthquake but also seismic hazard assessments. At present, there were two methods usually employed to image the time-space distribution of an earthquake rupture: one is finite-fault modeling (e.g., Lee et al. 2019), and the other is seismic-wave back-projection (e.g., Jian et al. 2019). Lee et al. (2019) constructed a complex finite-fault model of the 2018 Hualien earthquake and discovered that the outset of ruptures on the Milun fault had large slips at shallow depths near the land-sea interface. Subsequently, ruptures occurred in deeper areas, and then a relatively slow rupture velocity less than 2.0 km s^{-1} took place along the Milun fault. Such rupture variation appeared to be comparable with a surface vertical offset survey by Yen (2018) along the Milun fault. A result of P-wave back-projection, obtained by Jian et al. (2019), also displayed a slow rupture velocity, 1.85 - 2.0 km s^{-1}. In addition to the aforementioned methods, the source time function (STF) would also be a useful approach for investigating the complex ruptures of the source (e.g., Ruff and Kanamori 1983; Hwang 2013). The STF, which describes the ruptures of an earthquake from its initiation to its end, is a crucial source parameter in understanding an earthquake's rupture time history (e.g., Tanioka and Ruff 1997). In general, the STF is derived from the deconvolution of the mainshock and a reference earthquake (called empirical Green's function, EGF), which is usually an aftershock of the mainshock (Hartzell 1978). The EGF must be of much smaller magnitude relative to the mainshock. In addition, the focal mechanism and location of the EGF must be similar to those of the mainshock. The EGF could be also a synthetic wave, created in the position of the mainshock, to avoid inconsistency of the focal mechanism between the mainshock and EGF (e.g., Ruff and Kanamori 1983; Bilek et al. 2004; Ammon et al. 2006; Chu et al. 2009; Hwang 2013; Benz and Herrmann 2014). Through the STF, not only can the source rupture history be understood, but the source duration, seismic moment, radiated seismic energy, multiple sources, and static stress drop can be estimated (Bilek et al. 2004; Ammon et al. 2006; Hwang 2013; Vallée

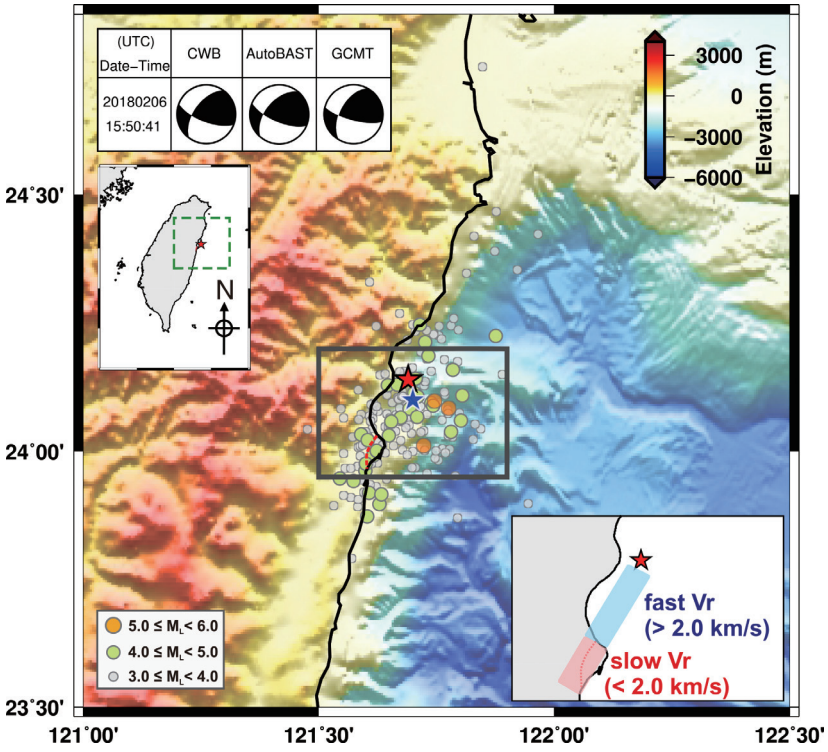

Fig. 1. Map showing the epicenter of the 2018 Hualien earthquake (star) and its aftershocks (circles). Blue star is the 1951 M_L 7.3 event. Orange circles are the aftershocks with $5.0 \le M_L < 6.0$; green circles, $4.0 \le M_L < 5.0$; grey circles, $3.0 \le M_L < 4.0$. Red dashed line indicates the Milun fault. Included also in this diagram are the focal mechanisms reported by the CWB, AutoBATS, and GCMT. The insert in the lower right denotes the rupture velocity (Vr) variation during the Hualien earthquake. The former rupture in sea (p1) has Vr > 2.0 km s^{-1}; the latter one (p2) on land has Vr < 2.0 km s^{-1}.

2013; Courboulex et al. 2016). The source parameters derived through the STF can also act as the primary input for ground-motion simulations in seismic hazard assessments (Graves et al. 2011). In this study, we used a non-negative time-domain deconvolution with smoothing constraints and damping to separate the STF from the teleseismic P-waves for the 2018 Hualien earthquake. For rapidly estimating the STF of the Hualien earthquake, only the stations with an azimuth normal to the rupture direction of the source were analyzed to negate the effect of rupture directivity.

2. DATA

The STFs were extracted from the teleseismic P-waves, which were provided by the IRIS DMC (Incorporated Research Institutions for Seismology Data Management Center). We selected seismic data with epicentral distances of 30 - 90° and a clear onset of P-waves. Prior to the deconvolution, the teleseismic P-waves were converted into displacements after removing instrument responses and then filtered between 0.01 and 1.0 Hz. To accelerate the deconvolution, we also downsampled the data to 0.1 s. Each teleseismic P-wave had a 35-s long, with 5 s before the P-onset and 30 s after the P-onset. In addition, for rapidly determining the STF of the 2018 Hualien earthquake, we used seismic data only from stations with an azimuth perpendicular to the rupture direction, which negated the effect of the rupture directivity of the source on the STF estimation (Fig. 2). The rupture direction of the Hualien earthquake was estimated to be N215°E from the average of fault plane strikes determined by the CWB centroid moment tensor (CMT), AutoBATS (Broadband Array in Taiwan for Seismology) CMT, and the GCMT (Global CMT) (also see Fig. 1).

3. METHOD

Let $g(t)$, $s(t)$, and $b(t)$ be the EGF, STF, and observed P-wave, respectively; then $g * s = b$, where the asterisk (*) denotes the convolution operator, and the integral of convolution is as follows:

$$\int_{-\infty}^{\infty} s(t)\, g(\tau - t) = b(t) \tag{1}$$

For finite data, Eq. (1) can be represented in a discrete form:

$$\sum_{i=0}^{m} s_i g_{k-i} \Delta t = b_k \tag{2}$$

where Δt is the sampling rate, m and n are the data points of $s(t)$ and $g(t)$, i is the time step, and $k = m + n + 1$. Equation (2) can be expressed in matrix form as follows:

$$\begin{bmatrix} g_1 & 0 & \cdots & \cdots & \cdots & 0 \\ g_2 & g_1 & & & & \vdots \\ \vdots & g_2 & \ddots & & & \vdots \\ \vdots & & \ddots & \ddots & & \vdots \\ g_{n-1} & & & \ddots & g_1 & 0 \\ g_n & \ddots & & & g_2 & g_1 \\ 0 & \ddots & \ddots & & & g_2 \\ \vdots & & \ddots & \ddots & & \vdots \\ \vdots & & & \ddots & \ddots & \vdots \\ \vdots & & & & \ddots & g_{n-1} \\ 0 & \cdots & \cdots & \cdots & 0 & g_n \end{bmatrix} \begin{bmatrix} s_1 \\ s_2 \\ \vdots \\ \vdots \\ \vdots \\ s_m \end{bmatrix} = \begin{bmatrix} b_1 \\ b_2 \\ \vdots \\ \vdots \\ \vdots \\ b_{n+m-1} \end{bmatrix} \tag{3}$$

Equation (3) can be rewritten in simple form as

$$GS = B \tag{4}$$

where G, S, and B are the matrices in Eq. (3) from left to right. In this study, we solved Eq. (4) through single-round inversion, which differs from the iterative time-domain deconvolution (Ammon et al. 2006; Chu et al. 2009; Benz and Herrmann 2014). For stably solving Eq. (4), we used non-negative solutions, smoothing constraints, and damping in the inversion process according to least-squares theory (cf. Lawson and Hanson 1974; Menke 2012). Thus, the final solution, S^{est}, of Eq. (4) was

$$S^{est} = (G^T G + \lambda^2 W^T W)^{-1} G^T B \tag{5}$$

where W is the smoothing matrix, which connects two nearby data points and is quantified by the second derivative (Menke 2012); W^T and G^T are the transpose matrices of W and G, respectively; λ^2 is the damping value. The superscript "-1" in Eq. (5) denotes the inverse matrix of $(G^T G + \lambda^2 W^T W)$. The damping value, related to $G^T G$, was a rather important factor in the inversion, and was defined as $\lambda^2 = C \times \frac{Tr(G^T G)}{Tr(W^T W)}$, where Tr denotes the trace of an square matrix and C is the damping factor, which must be carefully selected in the inversion (Press et al. 1992). We used the so-called L-curve (cf. Aster et al. 2012) to pick out the damping factor. Finally, an optimal damping factor of 100 was selected for the inversion.

The EGFs used in this study were synthetic teleseismic P-waves, calculated including direct P-waves and two depth phases (pP and sP waves) for a shallow source using a known focal mechanism, the IASP91 velocity model (Kennett and Engdahl 1991), and an attenuation factor t* = 1.0 for teleseismic P-waves (Okal 1992; Lin et al. 2006; Hwang et al. 2012). The EGFs without source duration were generated at the source position of the mainshock to avoid the inconsistence of location.

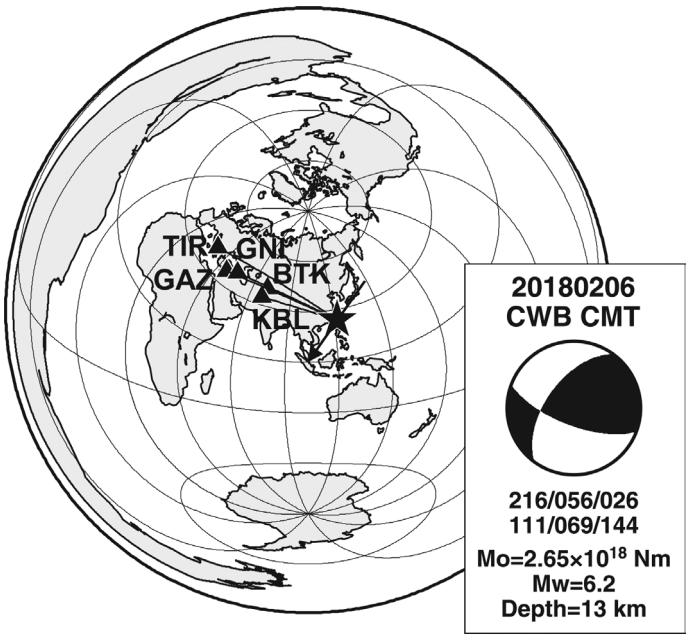

Fig. 2. Five stations with azimuth normal to the rupture direction (arrow) are used to perform non-negative time-domain deconvolution. Shown also is the focal mechanism determined by the CWB, which was used to generate synthetic P-waves, taken as the EGFs.

Because of the adopted time-domain deconvolution being a single-round inversion rather than the iterative time-domain deconvolution (e.g., Ammon et al. 2006; Chu et al. 2009), the deconvolved time function (DFT) included information not only from source but also from non-source along the entire time-axis (Fig. 3a). Intuitively, the front of the DFT was due to the source; the back of the DFT is not from the source. A long duration in the DFT would interpret excessively the observed data (Fig. 3a). Hence, to select an appropriate time-length from the DFT as the STF in the single-round inversion was necessary. Following information theory, we used the corrected Akaike information criteria (AICc) (Akaike 1974; McQuarrie and Tsai 1998) as an auxiliary to estimate the duration of the STF from the DFT. The AICc is defined as $\mathrm{AICc} = \ln\frac{RSS}{n} + \frac{n+k}{n-k-2}$, where *RSS* is the residual sum of squares between the observed and reconstructed P-waves, n is the number of data point (observed), and k denotes the number of model parameters (i.e., the selected time-length). The minimum AICc denoted the optimal model (i.e., time-length), selected to have a best interpretation on the observed data. In theory, the STF must be a continuous function, increasing from zero to a maximum value and decreasing to zero again (Udías et al. 2014). Hence, the continuity in the DFT would be an indicator in judging the STF. In addition, the selected STF also had to give a reasonable seismic moment. Figure 3 shows the time-domain deconvolution and the selection of time-length of the STF for station GAZ (also see Fig. 2). In Fig. 3a, the DFT had a discontinuity of time at 11.0 s, close to the time indicated by the AICc (9.9 s; Fig. 3b). In terms of the AICc, only using the first 10-s DFT would not result in overfitting between the observed and resulting P-waves (convolution of the EGF and selected STF). Additionally, the 11-s STF gave a seismic moment of 6.78×10^{18} Nm, comparable with 5.35×10^{18} Nm from USGS and 4.37×10^{18} Nm from GCMT. If we use the entire DFT, the estimated seismic moment will be 1.2×10^{19} Nm, an unreasonable value for the Hualien earthquake. According to the above-mentioned criteria, we finally determined the first 11-s DFT as the STF, which can also reconstruct most of the observed P-wave (Fig. 3a).

4. RESULTS

Because only stations with an azimuth perpendicular to the rupture azimuth were used to complete the STF analysis, the rupture azimuth first had to be determined. The aftershocks were distributed southwestward, which appeared to indicate that the 2018 Hualien earthquake ruptured toward the southwest from its epicenter (Fig. 1). The focal mechanisms determined by the CWB, AutoBATS, and GCMT all showed the fault plane to be a northwest-dipping plane with strikes of 208 - 220°, which correspond to the aftershock distribution; by contrast, the Milun fault dips in the opposite direction (Cheng et al. 1997; Shyu et al. 2016). Herein, whether the actual fault dipped eastward or westward was irrelevant because we only considered the rupture history for the earthquake along the rupture direction. Assuming that the northeast-to-southwest plane was the fault plane because of the aftershock distribution, the rupture azimuth was determined to be N215°E from the average of strikes determined

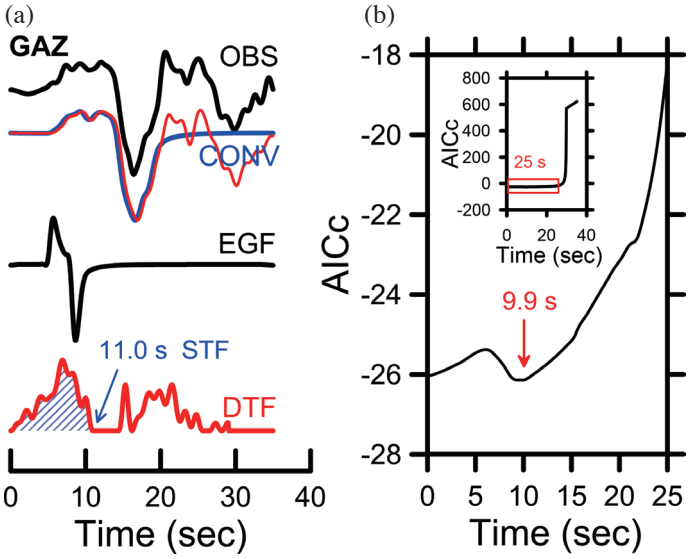

Fig. 3. (a) Example of non-negative time-domain deconvolution. (Upper) Observed P-wave (black line) and two resulting P-waves. Red line denotes the convolution of the EGF and DTF; blue one is the convolution of the EGF and the 11-s STF. (Middle) EGF created at the location of the mainshock by a known focal mechanism. (Lower) DFT (red line) extracted from the deconvolution of the observed P-wave and EGF. The 11-s STF (blue shading) is determined by using three criteria, including the continuity of the STF, the AICc, and the selected STF to give a reasonable seismic moment. For details, refer to the text. (b) The plot of AICc versus time (i.e., source duration) for the first 25 s shows a global minimum at 9.9 s. The insert displays the entire AICc distributed with time.

by the CWB, AutoBATS, and GCMT. Five stations met the criterion that the station azimuth was normal to the rupture direction, as displayed in Fig. 2. In this study, we produced the synthetic teleseismic P-waves without source duration at the location of mainshock as the EGF instead of the reference earthquakes (aftershocks or small-sized earthquakes around the mainshock; Hartzell 1978) (e.g., Ruff and Kanamori 1983; Bilek et al. 2004; Ammon et al. 2006; Chu et al. 2009; Hwang 2013; Benz and Herrmann 2014). The time-domain deconvolution can be regarded as a waveform inversion, so being controlled by large amplitudes in observations (Ruff and Kanamori 1983; Bilek et al. 2004). That is, a centroid depth used could be more suitable than an initial focal depth used in the time-domain deconvolution. Hence, an appropriate focal depth and focal mechanism used to generate the synthetic P-wave were necessary for the follow-up deconvolution. We tested focal depths from 1 to 30 km at 1-km intervals and three fault plane solutions (from CWB, AutoBATS, and GCMT; see also Fig. 1) in the deconvolution process. Figure 4a illustrates that the best results in the deconvolution was obtained using a focal depth of 9 km and the CWB's fault plane solutions (also see Fig. 2). The depth of 9 km estimated from this study was also comparable with those determined by moment tensors inversion from AutoBATS (10 km), CWB CMT (13 km), and GCMT (13.2 km). We averaged the STFs from the five stations to obtain the resultant STF (Fig. 4b). The misfit for each station in Fig. 4a was calculated through waveform fitting between the observed and resulting P-waves, obtained from the convolution of the EGF and resultant STF (averaged STF).

Figure 5a shows that the seismic moment rate varied with rupture time up to approximately 11 s, and then suggests that the 2018 Hualien earthquake should consist of several sub-events. Using forward multiple-event analysis (cf. Hwang 2013), we carefully decomposed the averaged STF (Fig. 4b) using triangular STFs and obtained at least six sub-events during the earthquake rupture. Given that all six sub-events occurred at a 9-km depth and had the same fault plane solutions, the synthetic P-waves generated from the six sub-events showed high consistencies with the observed ones up to 90% for these used stations (Fig. 5b). Table 1 lists the source parameters for the six sub-events. In Table 1, the seismic moment (M_0) for each sub-event was calculated from the area of the triangular STF, and the radiated seismic release (E_S) of each sub-event was determined using the method of Vassiliou and Kanamori (1982). Following a circular fault (Brune 1970, 1971), the static stress drop ($\Delta\sigma_S$) for each sub-event was derived by $\Delta\sigma_S = \frac{7M_0}{16}\left(\frac{2\pi f_c}{2.34\beta}\right)^3$, where β is the S-wave velocity in the source area and f_c is the corner frequency. f_c was defined as $f_c = \frac{2}{\pi T_{rup}}$ (Godano et al. 2015) for an isosceles triangular STF, where T_{rup} is the rupture time, 0.85 times the value of the source duration (width of the triangular STF) (cf. Heaton 1990). The average static stress drop ($\Delta\sigma_{S,ave}$) can be calculated by $\Delta\sigma_{S,ave} = \frac{\sum_{i=1}\Delta\sigma_{Si}M_{0i}}{\sum_{i=1}M_{0i}}$, where $\Delta\sigma_{Si}$ and M_{0i} are the static stress drop and seismic moment of the ith sub-event (Kanamori and Heaton 2000). The total M_0 and E_S were 6.48×10^{18} and 1.76×10^{14} Nm, respectively, with the ratio $E_S/M_0 = 2.72 \times 10^{-5}$. The average $\Delta\sigma_S$ was 5.03 MPa, determined by considering each sub-event's $\Delta\sigma_S$ weighted by M_0 itself (Kanamori and Heaton 2000; Ye et al. 2016).

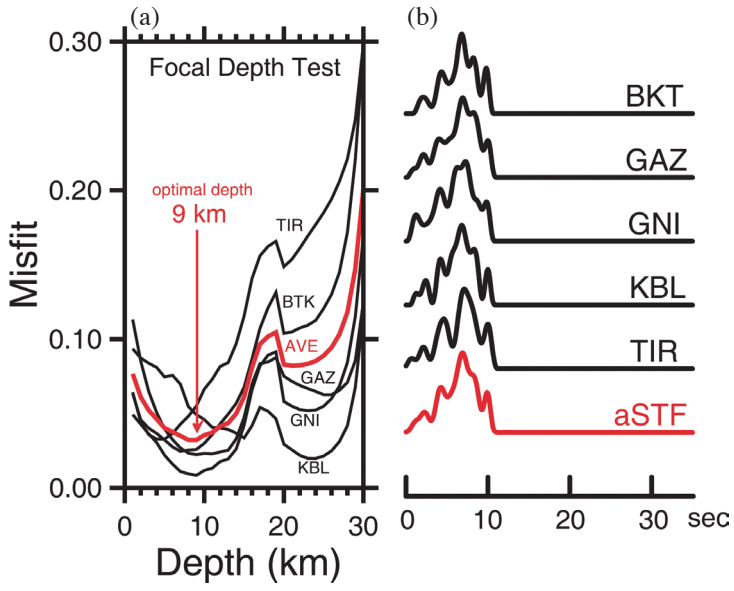

Fig. 4. (a) Misfit between the observed and resulting P-waves versus focal depth for the five investigated stations. Average misfit curve (AVE displayed by red line) denotes an optimal depth of 9 km. (b) The STFs derived from the five stations. Red line is the average STF.

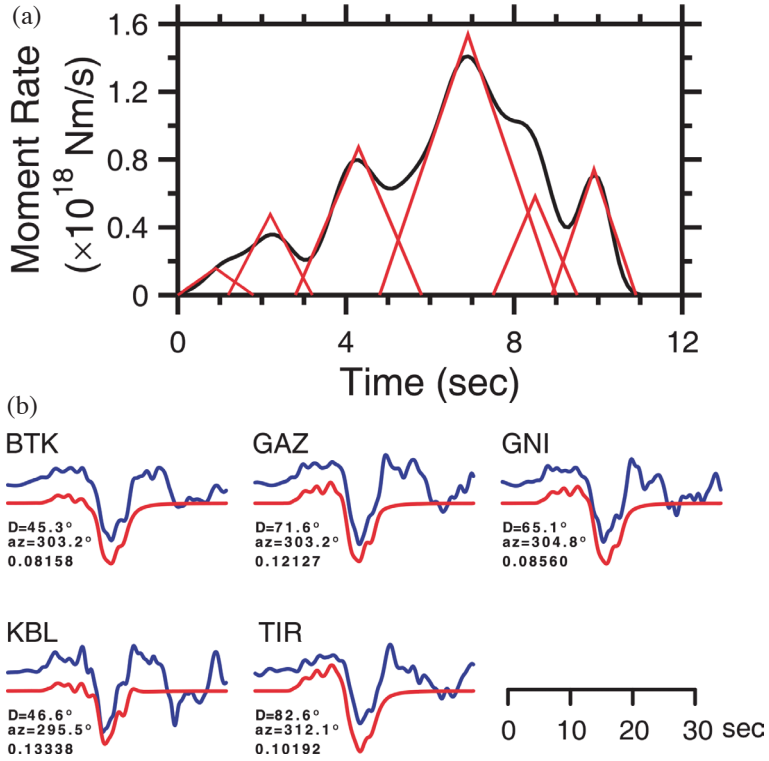

Fig. 5. (a) The STF (black line) of the 2018 Hualien earthquake, as displayed in Fig. 4b. A decomposition of the STF shows the mainshock to be composed of six sub-events (triangles). The source parameters of the sub-events are listed in Table 1. (b) Comparisons of the synthetic (red lines) and observed (blue lines) P-waves for the investigated stations. The synthetic P-waves are produced from the six sub-events. Also stated are the epicentral distance (D) in degrees, station azimuth (az) in degrees, and misfit between the synthetic and observed P-waves below each station.

Table 1. Multiple-source parameters for the 2018 Hualien earthquake.

No.	Focal mechanism (strike/dip/slip)	Source duration (sec)	Start time (sec)	M_0 (Nm)	E_S (Nm)	E_S/M_0	$\Delta\sigma_S$ (MPa)	M_w
1	216°/56°/26°	1.8	0	1.43×10^{17}	1.78×10^{12}	1.24×10^{-5}	2.30	5.4
2	216°/56°/26°	2.0	1.2	4.77×10^{17}	1.44×10^{13}	3.02×10^{-5}	5.59	5.7
3	216°/56°/26°	3.0	2.8	1.31×10^{18}	3.22×10^{13}	2.46×10^{-5}	4.56	6.0
4	216°/56°/26°	4.2	4.8	3.23×10^{18}	7.14×10^{13}	2.21×10^{-5}	4.09	6.3
5	216°/56°/26°	2.0	7.5	5.83×10^{17}	2.15×10^{13}	3.69×10^{-5}	6.84	5.8
6	216°/56°/26°	2.0	8.9	7.42×10^{17}	3.49×10^{13}	4.70×10^{-5}	8.70	5.9
Total		10.9		6.48×10^{18}	1.76×10^{14}	2.72×10^{-5}	5.03*	6.5

*Note: * This is an average $\Delta\sigma_S$ calculated by making $\Delta\sigma_S$ weighted by M_0 for each sub-event (cf. Kanamori and Heaton 2000).*

5. DISCUSSION

From the multiple-event analysis (Table 1 and Fig. 5), at least six sub-events constituted the 2018 Hualien earthquake, which had a total M_0 of 6.48×10^{18} Nm, corresponding to M_w = 6.5. The earthquake began with a sub-event of M_w = 5.4 and ended with one of M_w = 5.9. The largest sub-event, which had $M_0 = 3.22 \times 10^{18}$ Nm (M_w = 6.3) and a source duration of 4.2 s, occurred 4.8 s after the initiation of the earthquake. The total source duration was 10.9 s, slightly longer than that (9.7 s) estimated from an empirical moment-duration relation (Duputel et al. 2012) using the $M_0 = 6.48 \times 10^{18}$ Nm from this study. This might imply a lower average rupture velocity during the earthquake rupture. Following an empirical relationship between seismic moment and rupture length (Yen and Ma 2011), we derived a rupture length of approximately 21.2 km using $M_0 = 6.48 \times 10^{18}$ Nm. This indicates an approximate rupture velocity (Vr) of 1.94 km s^{-1}, which is 0.58 Vs, where Vs = 3.36 km s^{-1} is the crustal S-wave velocity. From the product $\Delta\sigma_S Vr^3$ = 29.3 MPa·km^3 s^{-3} for seismogenic earthquakes in Taiwan (Ruey-Der Hwang, unpublished manuscript), we obtained Vr = 1.80 km s^{-1} by using $\Delta\sigma_S$ = 5.03 MPa as in Table 1. In addition, Lee et al. (2019) and Jian et al. (2019) calculated Vr to be less than 2.0 km s^{-1} along the Milun fault from the finite-fault model and 1.85 - 2.0 km s^{-1} by an analysis of teleseismic P-wave back-projection, respectively. As mentioned above, on average, the rupture velocity for the Hualien earthquake is less than 2.0 km s^{-1} (~0.6 Vs), relatively slower than that (Vr ~ 0.8 - 0.9 Vs) for crustal earthquakes (cf. Kanamori and Heaton 2000). Table 1 and Fig. 5 show that the maximum moment rate occurred at 6.9 s, corresponding to a distance of approximately 13 km from the epicenter of the mainshock along the rupture direction using Vr = 1.94 km s^{-1}. This distance is located near the northernmost portion of the Milun fault on land (also see Fig. 1), i.e., near the land-sea interface. At the location, a field survey identified the largest vertical deformation on the surface (Yen 2018), and the finite-fault model showed large slips appearing at a shallow depth from Lee et al. (2019). Suppose that the maximum moment rate occurred at the northernmost portion of the Milun fault, to which the distance from the epicenter of the mainshock was ~15 km. To meet such distance, the rupture velocity in the sea area had to be faster up to ~2.2 km s^{-1}. This also implies a relatively slow rupture velocity traveling across the land since the average rupture velocity is less than 2.0 km s^{-1}. In other words, the rupture velocity varied from sea to land during the earthquake. Such variation might be associated with local velocity structures, where there is relatively lower velocity structures on land (Huang et al. 2014; Wen et al. 2019).

The total E_S of 1.76×10^{14} Nm obtained in this study was approximately three times larger than that estimated from the integral of velocity seismograms and reported by the IRIS (5.0×10^{13} Nm; http://ds.iris.edu/spud/eqenergy/16344247). Our higher E_S might indicate that high-frequency energy can be retrieved from the multiple-event analysis (e.g., Kikuchi and Fukao 1988; Hwang 2013). The largest E_S was in the third sub-event (Table 1); however, the fourth sub-event had the highest E_S/M_0 ratio. The ratio E_S/M_0, a dimensionless source parameter, is an important factor to account for the dynamic rupture features of an earthquake (Kanamori 1994). A large E_S/M_0 indicates a rapid drop in friction during earthquake faulting, whereas a small E_S/M_0 indicates a slower drop in friction (cf. Kanamori and Heaton 2000). From Table 1, E_S/M_0 varies with sub-events to reveal that the frictional strength on the fault was heterogeneous. This also resulted in variation in $\Delta\sigma_S$ during earthquake faulting. A sub-event with a large E_S/M_0 has a high $\Delta\sigma_S$; inversely, a sub-event with a small E_S/M_0 has a low $\Delta\sigma_S$ (Kanamori 1994; Kanamori and Heaton 2000). For simplification, we divide the 2018 Hualien earthquake faulting into two rupture processes; process 1 consisting of the first four sub-events, and process 2 composed of the last two sub-events. Process 1, occurring mostly in the sea area, had $\Delta\sigma_S$ ~ 4.3 MPa, whereas process 2, occurring in the land

area, had $\Delta\sigma_S \sim 7.9$ MPa. Apparently, the two ruptures thus had different $\Delta\sigma_S$, implying that the presence of water was the key factor that gave rise to the discrepancy in rupture processes from sea to land. From discussions as mentioned above, our finding appears to imply an inverse relationship between Vr and $\Delta\sigma_S$ during the 2018 Hualien earthquake. Of course, a detailed analysis of rupture directivity can provide further information regarding the rupture propagation in the 2018 Hualien earthquake. This analysis will be performed in our next study.

The E_S/M_0 ratio ($\sim 2.72 \times 10^{-5}$) and apparent stress (σ_a ~0.75 MPa) obtained in the present study are close to the values (3.0×10^{-5} and 1.0 MPa, respectively) determined by Ide and Beroza (2001) from a wide seismic moment distribution. Generally, the average $\Delta\sigma_S$ was calculated from M_0 and fault area (e.g., Ye et al. 2016). Likewise, the average $\Delta\sigma_S$ can be also estimated from the source duration of the complex STF after simplifying it into an isosceles triangle STF, i.e., as a single source (e.g., Tanioka and Ruff 1997; Bilek et al. 2004; Vallée 2013; Courboulex et al. 2016). However, this was likely to underestimate the value of $\Delta\sigma_S$. An alternative way was to use the multiple-event analysis by considering that $\Delta\sigma_S$ of each sub-event was weighted by M_0 itself to calculate the average $\Delta\sigma_S$ (Kanamori and Heaton 2000; Ye et al. 2016). The average $\Delta\sigma_S$ of the Hualien earthquake was calculated as 5.03 MPa, in agreement with the global observations (4 - 6 MPa) (e.g., Kanamori and Anderson 1975; Allmann and Shearer 2009; Ye et al. 2016). On average, the rupture parameters of the 2018 Hualien earthquake were similar to globally average values, but our detailed rupture analysis revealed inhomogeneous faulting during the earthquake.

6. CONCLUSIONS

Multiple-event analysis from the STF demonstrated heterogeneous ruptures during the 2018 Hualien earthquake, with E_S/M_0 and $\Delta\sigma_S$ varying between sub-events. The maximum moment rate of the STF occurred at 6.9 s, corresponding to a distance of approximately 13 km, where the ruptures entered the land. By taking the maximum moment rate in the STF as the demarcation of the rupture process, source ruptures implied higher Vr and lower $\Delta\sigma_S$ in the sea area relative to lower Vr and higher $\Delta\sigma_S$ in the land region. Seawater and local velocity structures were probably key factors behind these heterogeneous ruptures. On average, source parameters—including E_S/M_0, $\Delta\sigma_S$, and σ_a—for the Hualien earthquake were comparable with averages in global earthquake observations.

Acknowledgements We express our gratitude to the two anonymous reviewers for their critiques, which have enabled us to improve the manuscript significantly. We thank the IRIS for providing the GSN data to us, and the CWB for giving permission to use their earthquake catalog. Special thanks to Professors Ruey-Juin Rau and Tai-Lin Tseng, the Guest Editors, for handling the manuscript. The National Science Council, ROC, financially supported this study under Grant Nos. MOST105-2116-M-034-001 and MOST106-2116-M-034-002.

REFERENCES

Akaike, H., 1974: A new look at the statistical model identification. *IEEE Trans. Autom. Control*, **19**, 716-723, doi: 10.1109/tac.1974.1100705. [Link]

Allmann, B. P. and P. M. Shearer, 2009: Global variations of stress drop for moderate to large earthquakes. *J. Geophys. Res.*, **114**, B01310, doi: 10.1029/2008JB005821. [Link]

Ammon, C. J., A. A. Velasco, and T. Lay, 2006: Rapid estimation of first-order rupture characteristics for large earthquakes using surface waves: 2004 Sumatra-Andaman earthquake. *Geophys. Res. Lett.*, **33**, L14314, doi: 10.1029/2006GL026303. [Link]

Aster, R. C., B. Borchers, and C. H. Thurber, 2012: Parameter Estimation and Inverse Problems, 2nd Edition, Academic Press, Boston, 376 pp.

Benz, H. M. and R. B. Herrmann, 2014: Rapid estimates of the source time function and M_w using empirical Green's function deconvolution. *Bull. Seismol. Soc. Am.*, **104**, 1812-1819, doi: 10.1785/0120130325. [Link]

Bilek, S. L., T. Lay, and L. J. Ruff, 2004: Radiated seismic energy and earthquake source duration variations from teleseismic source time functions for shallow subduction zone thrust earthquakes. *J. Geophys. Res.*, **109**, B09308, doi: 10.1029/2004JB003039. [Link]

Brune, J. N., 1970: Tectonic stress and the spectra of seismic shear waves from earthquakes. *J. Geophys. Res.*, **75**, 4997-5009, doi: 10.1029/jb075i026p04997. [Link]

Brune, J. N., 1971: Correction to 'Tectonic stress and the spectra of seismic shear waves from earthquakes'. *J. Geophys. Res.*, **76**, 5002, doi: 10.1029/jb076i020p05002. [Link]

Cheng, S.-N., T.-T. Yu, Y.-T. Yeh, and C.-H. Chang, 1997: Relocation of the 1951 Hualien, Taitung earthquake sequence. Weather Analysis and Forecasting, Proceedings of Marine Meteorology and Seismology, in Commemoration of 100 Years of Weather Observation in the Taiwan Area, Taipei City, Taiwan, 690-699. (in Chinese with English abstract)

Chu, R., L. Zhu, and D. V. Helmberger, 2009: Determination of earthquake focal depths and source time functions in central Asia using teleseismic P waveforms. *Geophys. Res. Lett.*, **36**, doi: 10.1029/2009GL039494. [Link]

Courboulex, F., M. Vallée, M. Causse, and A. Chounet, 2016: Stress-drop variability of shallow earthquakes extracted from a global database of source

time functions. *Seismol. Res. Lett.*, **87**, 912-918, doi: 10.1785/0220150283. [Link]

Duputel, Z., L. Rivera, H. Kanamori, and G. Hayes, 2012: W phase source inversion for moderate to large earthquakes (1990-2010). *Geophys. J. Int.*, **189**, 1125-1147, doi: 10.1111/j.1365-246x.2012.05419.x. [Link]

Godano, M., P. Bernard, and P. Dublanchet, 2015: Bayesian inversion of seismic spectral ratio for source scaling: Application to a persistent multiplet in the western Corinth rift. *J. Geophys. Res.*, **120**, 7683-7712, doi: 10.1002/2015JB012217. [Link]

Graves, R., T. H. Jordan, S. Callaghan, E. Deelman, E. Field, G. Juve, C. Kesselman, P. Maechling, G. Mehta, K. Milner, D. Okaya, P. Small, and K. Vahi, 2011: CyberShake: a physics-based seismic hazard model for Southern California. *Pure Appl. Geophys.*, **168**, 367-381, doi: 10.1007/s00024-010-0161-6. [Link]

Hartzell, S. H., 1978: Earthquake aftershocks as Green's functions. *Geophys. Res. Lett.*, **5**, 1-4, doi: 10.1029/GL005i001p00001. [Link]

Heaton, T. H., 1990: Evidence for and implications of self-healing pulses of slip in earthquake rupture. *Phys. Earth Planet. Inter.*, **64**, 1-20, doi: 10.1016/0031-9201(90)90002-f. [Link]

Huang, H.-H., Y.-M. Wu, X. Song, C.-H. Chang, S.-J. Lee, T.-M. Chang, and H.-H. Hsieh, 2014: Joint Vp and Vs tomography of Taiwan: Implications for subduction-collision orogeny. *Earth Planet. Sci. Lett.*, **392**, 177-191, doi: 10.1016/j.epsl.2014.02.026. [Link]

Hwang, R.-D., 2013: Multiple event analysis of the 2008 M_w 7.9 Wenchuan earthquake: Implications for variations in radiated seismic energy during faulting. *Terr. Atmos. Ocean. Sci.*, **24**, 709-719, doi: 10.3319/TAO.2013.04.08.01(T). [Link]

Hwang, R.-D., T.-W. Lin, C.-C. Wu, W.-Y. Chang, and J.-P. Chang, 2012: Reexamining the source parameters of the 2010 M_L 6.4 JiaSian (Taiwan) earthquake using the inversion of teleseismic *P*-waves. *J. Asian Earth Sci.*, **48**, 24-30, doi: 10.1016/j.jseaes.2011.12.021. [Link]

Ide, S. and G. C. Beroza, 2001: Does apparent stress vary with earthquake size? *Geophys. Res. Lett.*, **28**, 3349-3352, doi: 10.1029/2001gl013106. [Link]

Jian, P.-R., S.-H. Hung, and L. Meng, 2019: Rupture behavior and interaction of the 2018 Hualien earthquake sequence and its tectonic implication. *Seismol. Res. Lett.*, **90**, 68-77, doi: 10.1785/0220180241. [Link]

Kanamori, H., 1994: Mechanics of earthquakes. *Annu. Rev. Earth Planet. Sci.*, **22**, 207-237, doi: 10.1146/annurev.ea.22.050194.001231. [Link]

Kanamori, H. and D. L. Anderson, 1975: Theoretical basis of some empirical relations in seismology. *Bull. Seismol. Soc. Am.*, **65**, 1073-1095.

Kanamori, H. and T. H. Heaton, 2000: Microscopic and macroscopic physics of earthquakes. In: Rundle, J. B., D. L. Turcotte, and W. Klein (Eds.), Geocomplexity and the Physics of Earthquakes, Geophysical Monograph Series, Volume 120, American Geophysical Union, Washington, D.C., 147-164, doi: 10.1029/GM120p0147. [Link]

Kennett, B. L. N. and E. R. Engdahl, 1991: Traveltimes for global earthquake location and phase identification. *Geophys. J. Int.*, **105**, 429-465, doi: 10.1111/j.1365-246X.1991.tb06724.x. [Link]

Kikuchi, M. and Y. Fukao, 1988: Seismic wave energy inferred from long-period body wave inversion. *Bull. Seismol. Soc. Am.*, **78**, 1707-1724.

Lawson, C. L. and R. J. Hanson, 1974: Solving Least Squares Problems, Prentice-Hall, 340 pp.

Lee, S.-J., T.-C. Lin, T.-Y. Liu, and T.-P. Wong, 2019: Fault-to-fault jumping rupture of the 2018 M_w 6.4 Hualien earthquake in eastern Taiwan. *Seismol. Res. Lett.*, **90**, 30-39, doi: 10.1785/0220180182. [Link]

Lin, T.-W., R.-D. Hwang, K.-F. Ma, and Y.-B, Tsai, 2006: Simultaneous determination of earthquake source parameters using far-field P waves: Focal mechanism, seismic moment, rupture length and rupture velocity. *Terr. Atmos. Ocean. Sci.*, **17**, 463-487, doi: 10.3319/TAO.2006.17.3.463(T). [Link]

McQuarrie, A. D. R. and C.-L. Tsai, 1998: Regression and Time Series Model Selection, World Scientific Pub. Co. Inc., 480 pp, doi: 10.1142/3573. [Link]

Menke, W., 2012: Geophysical Data Analysis: Discrete Inverse Theory, Academic Press, London, 330 pp, doi: 10.1016/C2011-0-69765-0. [Link]

Okal, E. A., 1992: A student's guide to teleseismic body wave amplitudes. *Seismol. Res. Lett.*, **63**, 169-180, doi: 10.1785/gssrl.63.2.169. [Link]

Press, W. H., B. P. Flannery, S. A. Teukolsky, and W. T. Vetterling, 1992: Numerical Recipes, Cambridge University Press, New York, 963 pp.

Ruff, L. and H. Kanamori, 1983: The rupture process and asperity distribution of three great earthquakes from long-period diffracted P-waves. *Phys. Earth Planet. Inter.*, **31**, 202-230, doi: 10.1016/0031-9201(83)90099-7. [Link]

Shyu, J. B. H., Y.-R. Chuang, Y.-L. Chen, Y.-R. Lee, and C.-T. Cheng, 2016: A new on-land seismogenic structure source database from the Taiwan Earthquake Model (TEM) project for seismic hazard analysis of Taiwan. *Terr. Atmos. Ocean. Sci.*, **27**, 311-323, doi: 10.3319/TAO.2015.11.27.02(TEM). [Link]

Tanioka, Y. and L. J. Ruff, 1997: Source time functions. *Seismol. Res. Lett.*, **68**, 386-400, doi: 10.1785/gssrl.68.3.386. [Link]

Udías, A., R. Madariaga, and E. Buforn, 2014: Source Mechanisms of Earthquakes: Theory and Practice, Cambridge University Press, 302 pp, doi: 10.1017/CBO9781139628792. [Link]

Vallée, M., 2013: Source time function properties indicate a

strain drop independent of earthquake depth and magnitude. *Nat. Comm.*, **4**, doi: 10.1038/ncomms3606. [Link]

Vassiliou, M. S. and H. Kanamori, 1982: The energy release in earthquakes. *Bull. Seism. Soc. Am.*, **72**, 371-387.

Wen, S., Y.-Y. Wen, K.-E. Ching, Y.-L. Yeh, and Y.-H. Lee, 2019: Tectonic implications on the 2018 Hualien earthquake. *Terr. Atmos. Ocean. Sci.*, **30**, 389-398, doi: 10.3319/TAO.2019.01.28.01. [Link]

Ye, L., T. Lay, H. Kanamori, and L. Rivera, 2016: Rupture characteristics of major and great ($M_w \geq 7.0$) megathrust earthquakes from 1990 to 2015: 1. Source parameter scaling relationships. *J. Geophys. Res.*, **121**, 826-844, doi: 10.1002/2015JB012426. [Link]

Yen, J. Y., 2018: Hualien earthquake sequence: Surface and remote sensing observations. Academic Seminar of the 0206 Hualien Earthquake Sequence, Central Weather Bureau, Taipei City, Taiwan. (in Chinese)

Yen, Y.-T. and K.-F. Ma, 2011: Source-scaling relationship for M 4.6-8.9 earthquakes, specifically for earthquakes in the collision zone of Taiwan. *Bull. Seismol. Soc. Am.*, **101**, 464-481, doi: 10.1785/0120100046. [Link]